

ORTHOGONAL BASES FOR VERTEX-MAPPED PYRAMIDS

JESSE CHAN* AND T. WARBURTON*

Abstract. Discontinuous Galerkin (DG) methods discretized under the method of lines must handle the inverse of a block diagonal mass matrix at each time step. Efficient implementations of the DG method hinge upon inexpensive and low-memory techniques for the inversion of each dense mass matrix block. We propose an efficient time-explicit DG method on meshes of pyramidal elements based on the construction of a semi-nodal high order basis, which is orthogonal for a class of transformations of the reference pyramid, despite the non-affine nature of the mapping. We give numerical results confirming both expected convergence rates and discuss efficiency of DG methods under such a basis.

1. Introduction. Mesh generation has not yet matured to the point where hexahedra-only meshes can be constructed for complex geometries. Despite this limitation, hexahedral elements remain popular, offering significant benefits over triangular and tetrahedral elements in high order finite element methods. For example, exploitation of the tensor-product structure allows for both simple constructions of basis functions and cubature rules, as well as fast, low-memory applications of high order operators. An alternative to purely hexahedral meshes are hex-dominant meshes [1, 23], which contain primarily hexahedral elements but also a small number of tetrahedral, wedge (prism) and pyramid elements, where wedge and pyramid elements are used as “glue” elements to facilitate connections between hexahedral and tetrahedral elements [9, 3, 11, 15].

Finite elements for the pyramid have been available since the early 1990s [2, 28], though a rigorous construction of high order bases for the pyramid has been a more recent development. Nigam and Phillips constructed conforming exact sequence finite element spaces in [21, 22], and Bergot, Cohen, and Duruffe gave explicit orthogonal bases on the pyramid [4, 3]. Both groups showed that, in addition to polynomials, the approximation spaces on the pyramid must contain rational functions in order for the trace spaces on the faces of the pyramid to remain polynomial, which is necessary for conformity of the global finite element space.

1.1. Techniques for efficient mass matrix inversion. In [16], it was shown that the computational structure of DG methods makes them well-suited for accelerators such as graphics processing units (GPUs). Under time-explicit DG methods, a block diagonal mass matrix inverse is accounted for at each timestep. A key observation for straight-edged simplicial elements is that each block of the mass matrix is a constant scaling of the mass matrix over a reference simplex. As a result, it is possible to sidestep the inversion of the full mass matrix by using derivative and lift operators which are premultiplied by the inverse of the reference mass matrix and applying local scalings. This sidesteps the storage and inversion of individual mass matrices over each element, which, due to the limited memory and reduced efficiency of general linear algebra routines on GPUs, is not expected to perform well on such accelerators.

Finite element methods typically define coordinate mappings from a reference to physical element using basis functions on the pyramid. Entries of the mass matrix are then computed on the reference element using a change of variables factor. For affine mappings of the reference simplex, this factor is constant, implying that only one mass matrix needs to be stored and inverted for all such simplices. For trilinear mapped tensor product hexahedral elements, this factor is no longer constant, but it is possible to decompose the mapped mass matrix into the Kronecker product of 1D mass matrices such that this factor is constant in each tensor product direction. An alternative procedure is to employ Lagrange polynomials at Gauss-Legendre-Lobatto (GLL) quadrature points and construct the lumped mass matrix through inexact numerical integration. This yields the Spectral Element Method (SEM), which boasts a trivially invertible diagonal mass matrix whose entries are the GLL quadrature weights.

Bedrosian introduced in [2] low order vertex shape functions for the pyramid which are rational in nature. Using such shape functions, transformations of the reference pyramid could be defined in terms of vertex positions of the physical pyramid. We consider in this work physical pyramids which are images of the reference pyramid under such a map, and refer to these as *vertex-mapped* pyramids, which are analogous to affine mappings of the simplex and trilinear mappings of the hexahedra.

*Department of Computational and Applied Mathematics, Rice University, 6100 Main St, Houston, TX, 77005

For vertex-mapped pyramids, however, we do not observe the advantages of either simplicial or hexahedral elements. The construction of lumped mass matrices and GLL quadratures for non-hexahedral elements is nontrivial [20], and the tensor product structure is absent for the pyramid. An analogue to GLL points may not even exist for non-hexahedral domains — Helenbrook showed that, on triangles, there does not exist a Lobatto-type quadrature rule which is both exact for polynomials of order $2N - 1$ and has a number of points equal to the dimension of order N polynomials [13]. Furthermore, in addition to the fact that a non-planar pyramid base produces a non-affine mapping, it was shown in [3] that for non-parallelogram pyramid bases, the mapping is not only non-affine, but rational in the r, s, t coordinates.

Attempts to rectify the costs and complications of non-affine mapped elements have also been proposed previously in the context of curvilinear meshes. Several methods have experimented with modifying the numerical method or formulation in order to sidestep difficulties in dealing with curvilinear and non-affine transformations. For example, Krivodonova and Berger [17] extrapolate boundary conditions on curvilinear boundaries to the boundary of a mesh consisting of affine-mapped triangles. However, while this technique allows for the efficient inversion of mass matrices on simplices where the determinant of the Jacobian is constant, it does not circumvent the presence of non-affine mappings for pyramids.

Warburton proposed in [24, 25] a Low-Storage Curvilinear discontinuous Galerkin method (LSC-DG), where the local basis functions on each element are taken to be the reference element basis functions divided by the square root of the change of variables factor over that element. As a result, the mass matrix is identical to the reference element mass matrix for all elements, independent of the local mapping. The analysis in [25] includes a convergence analysis with sufficient conditions requiring elements to be asymptotically affine to attain design order convergence. These conditions do not hold for general vertex-mapped pyramids, and it was observed in [4] that the LSC-DG error stagnated under refinement of pyramidal meshes.

We present here an alternative low-memory DG method by constructing a basis which yields a diagonal mass matrix for arbitrary vertex-mapped pyramids, but spans the same space as the optimal pyramid spaces described in [3] and [21]. The resulting DG method on vertex-mapped pyramidal meshes provides both efficient inversion of the mass matrix and optimal rates of convergence for high order approximation spaces. Numerical results confirm the accuracy and efficiency of this basis compared to LSC-DG and matrix-free alternatives, and computational experiments are performed to assess the performance of DG on GPUs.

2. High order finite elements on the pyramid. We introduce the bi-unit right pyramid $\hat{\mathcal{P}}$ with coordinates r, s, t such that

$$r, s \in [-1, -t], \quad t \in [-1, 1].$$

We also define the Duffy-type mapping from the bi-unit cube to the bi-unit right pyramid with coordinates $a, b, c \in [-1, 1]$

$$r = (1 + a) \left(\frac{1 - c}{2} \right) - 1, \quad s = (1 + b) \left(\frac{1 - c}{2} \right) - 1, \quad t = c.$$

which has a change of variables factor of $((1 - c)/2)^2$. The inverse transform is given by

$$a = \frac{2(1 + r)}{1 - t} - 1, \quad b = \frac{2(1 + s)}{1 - t} - 1, \quad c = t.$$

Quadrature rules for the pyramid may also be constructed by defining a quadrature rule on the bi-unit cube and applying the transform to the reference element.

The vertex functions of Bedrosian [2] are defined as follows on the bi-unit right pyramid:

$$\begin{aligned} v_1(r, s, t) &= \frac{(r + t)(s + t)}{2(1 - t)}, & v_2(r, s, t) &= -\frac{(r + t)(s + 1)}{2(1 - t)}, & v_3(r, s, t) &= -\frac{(r + t)(s + t)}{2(1 - t)}, \\ v_4(r, s, t) &= \frac{(r + 1)(s + 1)}{2(1 - t)}, & v_5(r, s, t) &= \frac{1 + t}{2}. \end{aligned}$$

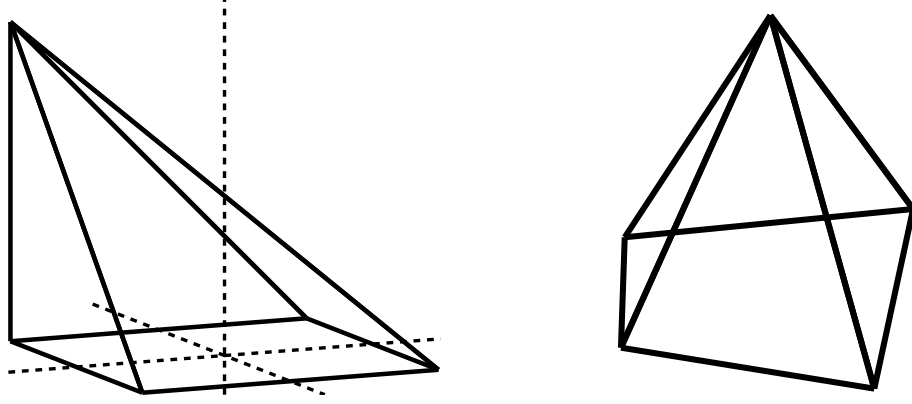


FIG. 2.1. The reference bi-unit right pyramid (left) and an example of a vertex-mapped pyramid (right).

The mapping $(x, y, z) = \mathbf{F}(r, s, t)$ from the reference pyramid $\widehat{\mathcal{P}}$ to the physical vertex-mapped pyramid \mathcal{P} is then given by

$$\mathbf{F}(r, s, t) = \sum_{i=1}^5 \mathbf{V}_i v_i(r, s, t),$$

where \mathbf{V}_i is the coordinate of the i th vertex of the physical pyramid. We also define J , the determinant of the Jacobian of \mathbf{F} , such that

$$J = \begin{vmatrix} \frac{\partial \mathbf{F}_x}{\partial r} & \frac{\partial \mathbf{F}_x}{\partial s} & \frac{\partial \mathbf{F}_x}{\partial t} \\ \frac{\partial \mathbf{F}_y}{\partial r} & \frac{\partial \mathbf{F}_y}{\partial s} & \frac{\partial \mathbf{F}_y}{\partial t} \\ \frac{\partial \mathbf{F}_z}{\partial r} & \frac{\partial \mathbf{F}_z}{\partial s} & \frac{\partial \mathbf{F}_z}{\partial t} \end{vmatrix}, \quad \int_{\mathcal{P}} u \, dx \, dy \, dz = \int_{\widehat{\mathcal{P}}} u J \, dr \, ds \, dt.$$

Bergot, Cohen, and Duruflé [3] defined an orthonormal basis on the bi-unit right pyramid as follows: let $P_i^{\alpha, \beta}$ be the Jacobi polynomial with weights α, β . Then, define ψ_{ijk}

$$\psi_{ijk}(a, b, c) = \sqrt{2^{2\mu_{ij}+2}} P_i^{0,0}(a) P_i^{0,0}(b) \left(\frac{1-c}{2} \right)^{\mu_{ij}} P_k^{2\mu_{ij}+2}(c), \quad (2.1)$$

where $\mu_{ij} = \max(i, j)$ and $k \leq N - \mu_{ij}$. Under the Duffy-type mapping from (a, b, c) to (r, s, t) coordinates, these ψ_{ijk} form an orthonormal basis over the reference bi-unit right pyramid.

The elements of the mass matrix for the mapped pyramid \mathcal{P} are defined as

$$M_{ijk, i'j'k'} = \int_{\widehat{\mathcal{P}}} \psi_{ijk} \psi_{i'j'k'} J \, dx = \int_{-1}^1 \int_{-1}^1 \int_{-1}^1 \psi_{ijk} \psi_{i'j'k'} \left(\frac{1-c}{2} \right)^2 J \, da \, db \, dc.$$

For the orthonormal basis of Bergot, Cohen, and Duruflé, the mass matrix is no longer diagonal under a non-affine mapping, and inversion of the mass matrix must be done individually over every element. However, while it is difficult to define an orthonormal basis for an arbitrary non-affine map, it is possible to derive an orthogonal basis for a vertex-mapped transformation of the reference pyramid.

2.1. An orthonormal semi-nodal basis on the mapped element. We first restate Lemma 3.5 of Bergot, Cohen, and Duruflé [3], which gives that the determinant of the Jacobian J is bilinear when mapped under the inverse Duffy-type transform to the bi-unit cube.

Lemma 2.1. Let Q_{N_a, N_b, N_c} be the space of polynomials of individual orders N_a , N_b , and N_c in the a, b, c coordinates on the bi-unit cube, and let J be the determinant of the Jacobian mapping. Then, $J \in Q_{1,1,0}$ for vertex-mapped transformations of the pyramid.

We may use this fact, along with the fact that the $N+1$ point Gauss-Legendre quadrature rule integrates exactly polynomials of degree $2N+1$, to construct an orthonormal basis for the vertex-mapped pyramid (we will refer to this as the *semi-nodal* basis). To begin, we first show a property of Jacobi polynomials with varying weights.

Lemma 2.2. For $i \neq j$,

$$\int_{-1}^1 \left(\frac{1-c}{2} \right)^{2+(N-i)+(N-j)} P_i^{2N+3-2i,0}(c) P_j^{2N+3-2j,0}(c) dc = C_i^N \delta_{ij},$$

where

$$C_i^N = \frac{N+2}{2^{2(N+1-i)}(2N+3-2i)}.$$

Proof. Assume without loss of generality that $j < i$ and that $N, i > 0$ (since P_0 is trivially determined for any choice of N). The statement of the Lemma is then equivalent to showing

$$\int_{-1}^1 \left(\frac{1-c}{2} \right)^{2+(N-i)+(N-j)} P_i^{2N+3-2i,0}(c) p_j(c) dc = 0$$

for any polynomial $p_j(c)$ of degree j . Since $j < i$, we may take

$$p_j(c) = \left(\frac{1-c}{2} \right)^j, \quad j = i-1-k$$

for $i > k > 0$. Then,

$$\begin{aligned} & \int_{-1}^1 \left(\frac{1-c}{2} \right)^{2+2(N-i)+(N-j)} P_i^{2N+3-2i,0}(c) \left(\frac{1-c}{2} \right)^j dc \\ &= \int_{-1}^1 \left(\frac{1-c}{2} \right)^{2N+3-2i} P_i^{2N+3-2i,0}(c) \left(\frac{1-c}{2} \right)^k dc = 0, \end{aligned}$$

due to the weighted orthogonality of Jacobi polynomials to polynomials of lower order. Finally, when $i = j$, we may compute

$$C_i^N = \int_{-1}^1 \left(\frac{1-c}{2} \right)^{2+2N-2i} \left(P_i^{2N+3-2i,0}(c) \right)^2 dc = \frac{N+2}{2^{2(N+1-i)}(2N+3-2i)}.$$

□

A similar property was also exploited by Beuchler and Schöberl in [5] to construct basis functions for the triangle with sparse stiffness matrices. These polynomials are shown in Figure 2.1 for $N = 3$. Note also that a change of index from i, j to $(N-i), (N-j)$ in the above proof gives

$$\int_{-1}^1 \left(\frac{1-c}{2} \right)^{2+i+j} P_{N-i}^{2i+3,0}(c) P_{N-j}^{2j+3,0}(c) dc = C_{N-i}^N \delta_{ij}, \quad C_{N-i}^N = \frac{N+2}{2^{2i+2}(2i+3)}.$$

We may now construct a semi-nodal basis which is orthogonal on vertex-mapped pyramids by relying on the fact that the determinant of the Jacobian is bilinear in a, b constant in c .

Lemma 2.3. Let a_i^k, b_j^k denote $(k+1)$ -point Gauss-Legendre quadrature points with corresponding weights w_i^k, w_j^k . Let \mathcal{P} be a vertex-mapped pyramid, and let ϕ_{ijk} be defined on the bi-unit cube as

$$\phi_{ijk}(a, b, c) = \ell_i^k(a) \ell_j^k(b) \left(\frac{1-c}{2} \right)^k P_{N-k}^{2k+3}(c),$$

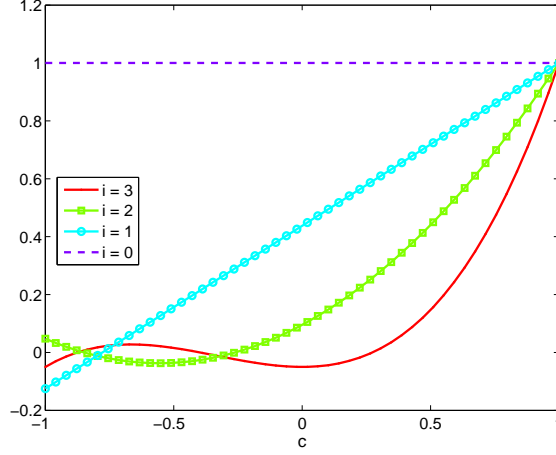


FIG. 2.2. Polynomials $P_i^{2N+3-2i}(c)$ for $N = 3$, normalized by their value at $c = 1$.

where ℓ_i^k is the order k Lagrange polynomial which is zero at all but the i th $(k+1)$ Gauss-Legendre nodes, and $P_{N-k}^{2k+3}(c)$ is the Jacobi polynomial of degree k with order-dependent weight $2k+3$. Then, the ϕ_{ijk} are orthogonal with respect to the L^2 inner product over \mathcal{P} , and the entries of the mass matrix are

$$M_{ijk,ijk} = J_{ijk} w_i^k w_j^k C_{N-k}^N$$

where J_{ijk} is the determinant of the Jacobian evaluated at quadrature points a_i^k, b_j^k .

Proof. Assume without loss of generality that $k \geq k'$. By Lemma 2.1, the tensor product of $(k+1)$ -point Gauss-Legendre quadrature rules integrates exactly

$$\int_{-1}^1 \int_{-1}^1 J \ell_i^k(a) \ell_{i'}^{k'}(a) \ell_j^k(b) \ell_{j'}^{k'}(b) da db.$$

The entries of the mass matrix are then

$$\begin{aligned} M_{ijk,i'j'k'} &= \int_{\mathcal{P}} \phi_{ijk} \phi_{i'j'k'} J dx = \int_{-1}^1 \int_{-1}^1 \int_{-1}^1 \phi_{ijk} \phi_{i'j'k'} \left(\frac{1-c}{2} \right)^2 J da db dc \\ &= \sum_{l=0}^k \sum_{m=0}^k w_l^k w_m^k \ell_i^k(a_l^k) \ell_{i'}^{k'}(a_l^k) \ell_j^k(b_m^k) \ell_{j'}^{k'}(b_m^k) J_{lmk} \\ &\quad \times \int_{-1}^1 P_{N-k}^{2k+3,0}(c) P_{N-k'}^{2k+3',0}(c) \left(\frac{1-c}{2} \right)^{2+k+k'} dc \\ &= \sum_{l=0}^k \sum_{m=0}^k J_{lmk} \delta_{il} \delta_{ii'} \delta_{jm} \delta_{jj'} w_l^k w_m^k C_{N-k}^N \delta_{kk'} \\ &= J_{lmk} \delta_{ii'} \delta_{jj'} w_l^k w_m^k C_{N-k}^N \delta_{kk'}. \end{aligned}$$

where the integral over c yields $C_{N-k}^N \delta_{kk'}$ by Lemma 2.2. \square

Figure 2.3 shows $\ell_i^k(a) \ell_j^k(b)$, the basis in a, b . The tensor product in the c direction of these Lagrange polynomials with the weighted Jacobi polynomials in Figure 2.1 produces the orthogonal semi-nodal basis described in Lemma 2.3.

Lemma 2.4. *The semi-nodal basis defined by ϕ_{ijk} for $0 \leq k \leq N$ and $0 \leq i, j \leq N-k$ spans the same approximation space as that of the orthonormal rational basis ψ_{ijk} in Equation (2.1).*

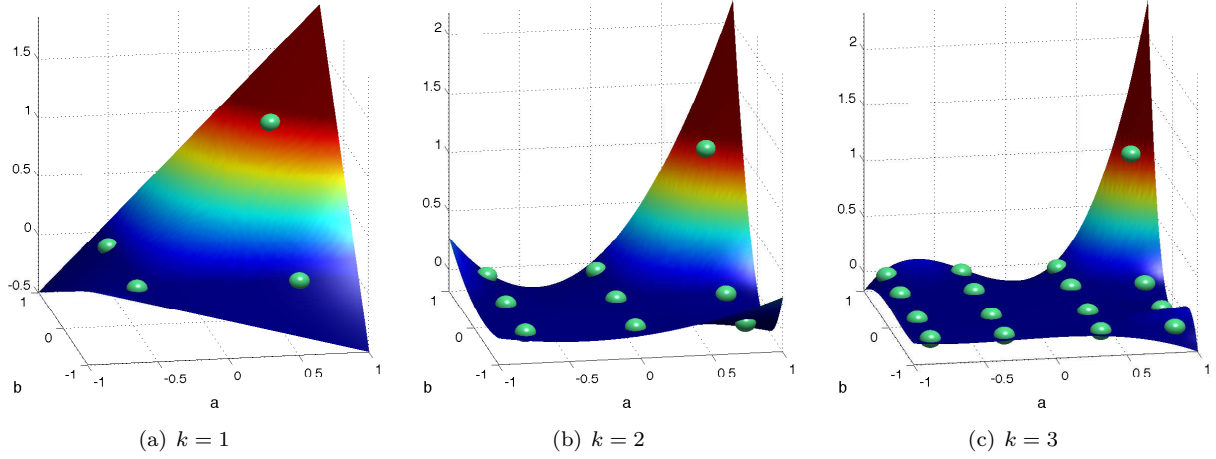


FIG. 2.3. Polynomials $\ell_i^k(a)\ell_j^k(b)$ for $N = 3$, shown with Gauss-Legendre points overlaid.

Proof. From Proposition 1.8 of [3], the orthonormal rational basis on the bi-unit cube ψ_{ijk} spans the space

$$Q_N = \sum_{k=0}^N Q_k(a, b)(1 - c)^k,$$

where $Q_k(a, b)$ consists of polynomials of order k in both a and b . Since $\ell_i^k(a)\ell_j^k(b)$ spans $Q_k(a, b)$, and $Q_k(a, b) \supset Q_{k-1}(a, b) \supset \dots$, we need only to show that

$$\text{span} \left\{ \left(\frac{1 - c}{2} \right)^k P_{N-k}^{2k+3}(c), \quad k = 0, \dots, N \right\} = \text{span} \left\{ (1 - c)^k, \quad k = 0, \dots, N \right\} = P_N(c),$$

where $P_N(c)$ is the space of polynomials of degree N in c . Since $(1 - c/2)^k P_{N-k}^{2k+3}(c)$ is a polynomial of total degree N , it is automatically contained in $P_N(c)$, and it remains to prove the opposite inclusion. Using a counting argument and the fact that P_N has dimension $N + 1$, we may prove the opposite inclusion by showing linear independence of $(1 - c)^k P_{N-k}^{2k+3}(c)$, or equivalently $(1 - c)^{N-k} P_k^{2N+3-2k}(c)$ for $0 \leq k \leq N$.

Since $P_k^{2N+3-2k}(c)$ has leading order term c^k , it is sufficient to show that $(1 - c)^{N-k} c^k$ is linearly independent. Using the binomial theorem, we may expand

$$(1 - c)^{N-k} c^k = \sum_{i=0}^{N-k} (-1)^i \binom{N-k}{i} c^{i+k}.$$

The lowest order term in the above sum is c^k ; since this term is distinct for each $0 \leq k \leq N$, this implies linear independence of $(1 - c)^{N-k} c^k$. \square

The existence of an L^2 orthogonal basis on the vertex-mapped pyramid also allows us to characterize the spectra of the mass matrix more precisely.

Corollary 2.5. *The minimum and maximum eigenvalues of the mapped mass matrix under the rational basis (2.1) are given by*

$$\lambda_{\min} = J_{\min}, \quad \lambda_{\max} = J_{\max}$$

where J_{\min}, J_{\max} are the minimum and maximum values of the determinant of the Jacobian, evaluated at the tensor product $(N + 1)^2$ -point Gauss-Legendre quadrature on the base of the pyramid.

Proof. Let M_r be the mass matrix constructed using the rational basis (2.1), and let M be the mass matrix constructed using the semi-nodal basis. Scaling ϕ_{ijk} by $w_i^k w_j^k C_{N-k}^N$ results in an orthonormal basis, implying that M is diagonal with entries equal to the values of J at quadrature points a_i^k, b_i^k . Lemma 2.4 then implies that there is a linear change of basis S from the rational basis ψ_{ijk} to the semi-nodal basis ϕ_{ijk} such that $M_r = S^{-1}MS$. Since M is diagonal, ϕ_{ijk} are eigenfunctions of the mass matrix with corresponding eigenvalues equal to the diagonal entries of M .

Since $J \in Q_{1,1,0}$ on the bi-unit cube, J is bilinear in $a, b \in [-1, 1]^2$. Since a bilinear function increases or decreases monotonically in a and b , the maximum and minimum values of J are attained at the points a_i^k, b_j^k closest to the boundary of $[-1, 1]^2$. Since a_i^k, b_j^k are given by the k th order Gauss-Legendre rule for $k \leq N+1$, and the extremal points of the k th order Gauss-Legendre quadrature approach -1 and 1 monotonically in k , the extremal values of J are attained for $k = N+1$.

We complete the proof by noting that the evaluation of the Jacobian factor J at fixed a_i^k, b_j^k is constant in c , so we may choose $c = -1$, which corresponds to the quadrilateral base of the pyramid. \square

3. Numerical results. We begin by comparing the semi-nodal basis constructed in Lemma 2.3 with two low-storage alternatives for mass matrix inversion — Chebyshev iteration [12] and the Low-Storage Curvilinear DG method [25]. We then demonstrate the efficiency of GPU-accelerated discontinuous Galerkin methods on vertex-mapped pyramidal elements using the new proposed basis.

3.1. Comparison with Chebyshev iteration. The Chebyshev iteration constructs an explicit matrix polynomial using recurrence relations for Chebyshev polynomials, and has experienced revived attention due to the fact that it may be formulated purely in terms of matrix-vector multiplications. This is in contrast to Conjugate Gradients, which requires inner products at each iteration. On parallel architectures where communication between processes is costly, this necessitates a reduction from a subset of parallel processes at each iteration. However, unlike Conjugate Gradients, the Chebyshev iteration requires a-priori knowledge of tight bounds on the spectrum of the matrix; poor estimates of the minimum and maximum eigenvalue may result in slow or stalled convergence.

The Chebyshev method has previously been used in the global inversion of continuous Galerkin mass matrices by Wathen and Rees [26], where eigenvalue bounds for the mass matrix were derived for linear and bilinear elements in 2D.

Suppose the spectra of the mass matrix is contained in $[\lambda_{\min}, \lambda_{\max}]$. Then, for the solution x to $Mx = b$, the k th Chebyshev iterate x_k satisfies

$$\|x - x_k\|_2 \leq \left(\frac{2\tau^k}{1 + \tau^{2k}} \right) \|x - x_0\|_2, \quad \tau = \frac{1 - \sqrt{\lambda_{\min}/\lambda_{\max}}}{1 + \sqrt{\lambda_{\min}/\lambda_{\max}}}.$$

This above error bound may also be rearranged to yield

$$\|x - x_k\|_2 \leq 2 \left(\frac{\sqrt{\kappa} - 1}{\sqrt{\kappa} + 1} \right)^k \|x - x_0\|_2, \quad (3.1)$$

where κ is the mass matrix condition number. Wathen observed that, for the symmetric, positive-definite mass matrix, the error bound for the Chebyshev iteration in (3.1) is nearly identical to the error bound for the Conjugate Gradients method; the only difference between the bound for Conjugate Gradients and (3.1) is the norm in which the error converges.

We consider Chebyshev iteration of the mapped mass matrix using the rational basis (2.1) of Bergot, Cohen, and Durufle. The bounds on the maximum and minimum eigenvalues of the matrix are given by Corollary 2.5, and are confirmed numerically. We construct a mapped pyramid by warping the quadrilateral base with displacement magnitude γ , as shown in Figure 3.1, along with the residual convergence of the Chebyshev iteration for various γ and the expected rate of convergence given by (3.1), which is observed to give an accurate estimate of the residual at each step. No significant change was observed in the convergence of the Chebyshev iteration with increasing N ; however, the results show that, even for a modestly warped pyramid, the iteration count is greater than 10, which is unacceptably high for the inversion of the mass

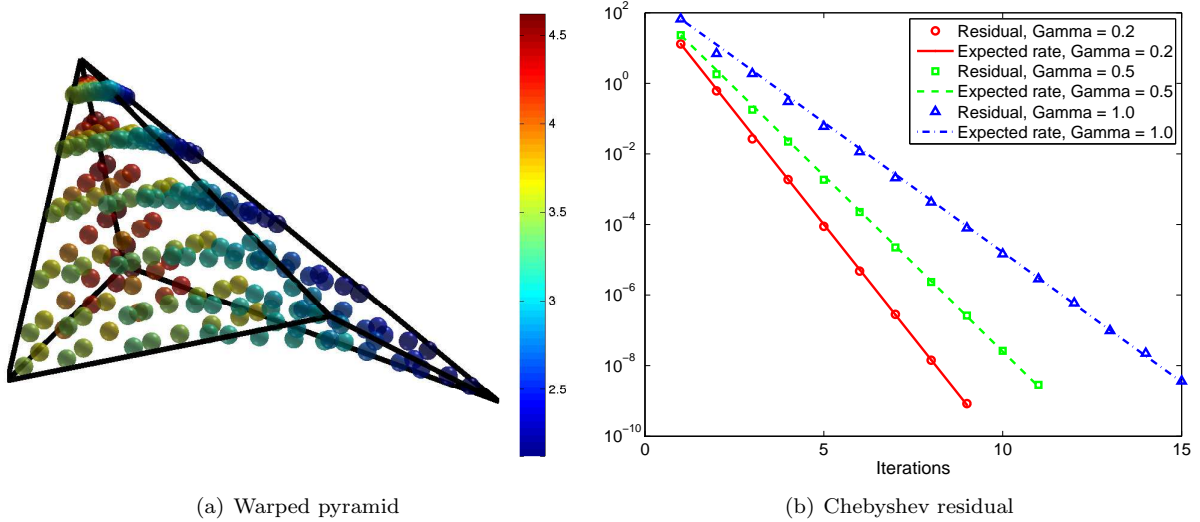


FIG. 3.1. A warped pyramid with $\gamma = 1$, overlaid with values of the Jacobian at quadrature points for $N = 5$ (left), and the convergence history of the Chebyshev iteration for various γ (right). The expected rate of convergence is given by (3.1).

matrix — an $O(10)$ iteration count is relatively low for steady state or time-implicit methods, where a small number of time steps are used, but is a high cost for explicit-time discontinuous Galerkin methods, which require multiple inversions of the mass matrix per time-step over millions of timesteps.

Various preconditioners for the Chebyshev iteration were tested, with mixed results. We observed that the diagonal of the mass matrix was constant under all vertex mappings of the pyramid, which rendered a Jacobi preconditioner ineffective. We tested also an incomplete Cholesky factorization with tolerance ϵ , which improved the number of iterations needed to reach convergence, but introduced additional memory costs for storing Cholesky factors for each element. Additionally, the tolerance ϵ required to achieve a fixed number of iterations was observed to depend on the magnitude of the displacement γ , implying that, for fixed ϵ , the effectiveness of incomplete Cholesky as a preconditioner would worsen as the shape regularity of the pyramid degrades. For architectures such as GPUs, where device memory is typically $O(10)$ gigabytes, such additional storage costs could decrease the maximum problem size by a large factor.

3.2. Comparison with LSC-DG. The Low-Storage Curvilinear DG method (LSC-DG) exploits the property of DG that local approximation spaces do not need to satisfy explicit conformity conditions. Warburton proposed the use of specific basis functions

$$\tilde{\phi}_i(x, y, z) = \frac{\phi_i(r, s, t)}{\sqrt{J}},$$

where ϕ_i is the basis function over the reference element \hat{K} , and J is the determinant of the mapping Jacobian for the physical element K . As a consequence, the entries of the mass matrix

$$M_{ij} = \int_K \tilde{\phi}_j \tilde{\phi}_i \, dx \, dy \, dz = \int_{\hat{K}} \frac{\phi_j \phi_i}{J} J \, dr \, ds \, dt = \int_{\hat{K}} \phi_j \phi_i \, dr \, ds \, dt$$

are simply the entries of the mass matrix over the reference element \hat{K} [24].

For isoparametric curvilinear mappings, J is polynomial, implying that $\tilde{\phi}_i$ is rational. Warburton showed that, under a scaling assumption on quasi-regular elements, using such basis functions incurs an additional constant in the bounds on the best approximation error between a function u and its weighted projection $\Pi_w u$. Given such an element K with size h and Jacobian determinant J , the projection error may be bounded as follows

$$\|u - \Pi_w u\|_{L^2(K)} \leq Ch^{N+1} \left\| \frac{1}{\sqrt{J}} \right\|_{L^\infty(K)} \left\| \sqrt{J} \right\|_{W^{N+1, \infty}(K)} \|u\|_{W^{N+1, 2}(K)}$$

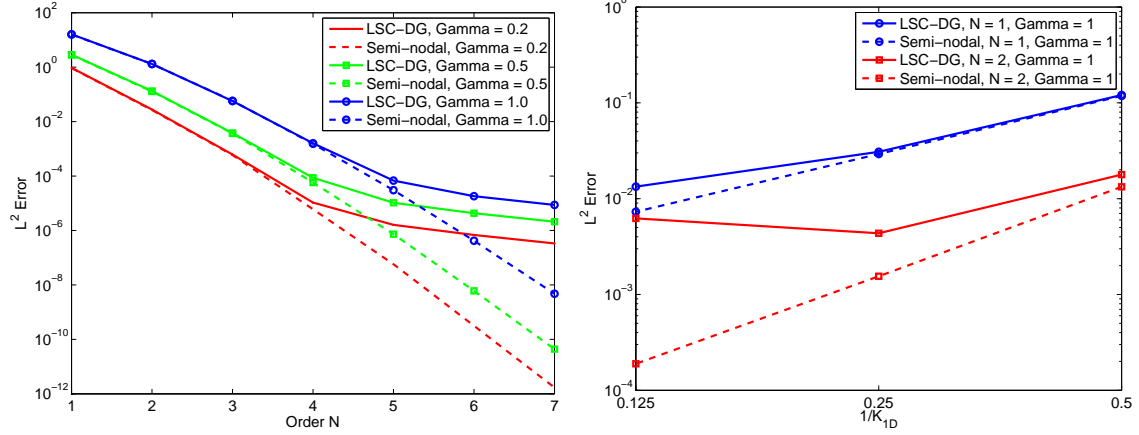


FIG. 3.2. L^2 projection errors for the LSC-DG and semi-nodal orthogonal pyramid bases under increasing N and various warpings of the reference pyramid (left), as well as under mesh refinement (right).

where $\|\cdot\|_{W^{N+1,\infty}(K)}$ denotes the L^∞ Sobolev norm of order $N+1$ over K . For comparison, the projection error bound for curvilinear mappings using standard mapped bases is

$$\|u - \Pi_w u\|_{L^2(K)} \leq Ch^{N+1} \left\| \frac{1}{\sqrt{J}} \right\|_{L^\infty(K)} \left\| \sqrt{J} \right\|_{L^\infty(K)} \|u\|_{W^{N+1,2}(K)}.$$

In other words, accuracy of approximation using rational LSC-DG basis functions comes with stricter requirements on the smoothness of the determinant of the Jacobian J .

Because the mapping for pyramids with non-parallelgram bases involves factors of $(1-t)^{-1}$, the derivative of the Jacobian mapping gains higher and higher inverse powers of $(1-t)$. Since the $W^{\infty,N+1}$ norm of \sqrt{J} is ill-defined due to this singularity, the bound on LSC-DG projection error does not hold, and we are not guaranteed convergence. To illustrate this, we compare projections of the smooth function

$$f(x, y, z) = \cosh(x + y + z)$$

on warped pyramids. L^2 projections using the LSC-DG pyramid basis and the semi-nodal basis of Lemma 2.3 are computed on both the warped element shown in Figure 3.1 for $\gamma = .2, .5, 1$, and on meshes of pyramid elements. These meshes are constructed by subdividing the bi-unit cube into $K_{ID} \times K_{ID} \times K_{ID}$ hexahedra, where K_{ID} is the number of subdivisions along each edge of the cube. Each hexahedra is then subdivided into 6 pyramids, and the pyramid vertex positions are perturbed randomly to ensure that the determinant of the mapping Jacobian is non-constant. L^2 errors are computed on each mesh at various orders of approximation N . Figure 3.2 shows the L^2 error for each basis under refinement in both h and N , with the convergence of the LSC-DG error stalling under refinement in each case. We note that Bergot, Cohen, and Durufle also observed that error stalled under mesh refinement for fixed order N . The shape regularity of the pyramid (which is controlled by γ) also affects the approximation error, but only by a constant factor.

4. Efficient discontinuous Galerkin methods on pyramids. Finally, to ascertain the effectiveness of the semi-nodal basis for discontinuous Galerkin methods, we examine numerical solutions of the advection equation and the acoustic wave equation using time-explicit DG.

4.1. Advection equation. We consider the advection equation on a bi-unit cube $[-1, 1]^3$ with periodic boundary conditions

$$\frac{\partial u}{\partial t} + \nabla \cdot (\beta u) = 0,$$

where β is a vector indicating direction of advection. We assume a mesh Ω_h consisting purely of pyramidal elements K . For each face of K , we refer to the outward normal as \mathbf{n} . Let $K \in \Omega_h$ denote a specific element,

and let u^-, v^- denote the trace of the solution u and a test function v , respectively, on a face. We may then define the jump $\llbracket u \rrbracket$ and average $\{u\}$ over a face as

$$\llbracket u \rrbracket = u^- - u^+, \quad \{u\} = \frac{u^- + u^+}{2}.$$

Let $\beta_n = \beta \cdot n$. Then, the semidiscrete discontinuous Galerkin formulation of the advection equation is given locally as

$$\int_K v^- \left(\frac{\partial u}{\partial t} + \nabla \cdot (\beta u) \right) dx + \int_{\partial K} \left(\frac{\beta_n - \alpha |\beta_n|}{2} \right) v^- \llbracket u \rrbracket dx = 0,$$

where α is a parameter. For $\alpha = 1$, an upwind numerical flux is recovered, while for $\alpha = 0$, a central flux is recovered [14]. The formulation is then discretized by representing u, v using the semi-nodal basis $\{\phi_i\}_{i=1}^{N_p}$ defined in Lemma 2.3. This results in a system of ODEs

$$\frac{du}{dt} + M^{-1} \left(\sum_{k=1}^3 S^k u + L^f F \right) = 0,$$

where L^f, S^k are the lift operator and weak derivative matrix defined by

$$L_{ij}^f = \int_{\partial K} \phi_i(x) \phi_j(x) dx \approx \sum_{l=1}^{N_c^f} w_l \phi_i(x_l) \phi_j(x_l)$$

$$S_{ij}^k = \int_K \phi_i(x) \beta_k(x) \frac{\partial \phi_j}{\partial x_k} dx \approx \sum_{l=1}^{N_c} w_l \phi_i(x_l) \beta_k(x_l) \frac{\partial \phi_j(x_l)}{\partial x_k},$$

and F_l is the flux at the quadrature point x_l . N_c and N_c^f denote the number of quadrature points for volume and surface integrals, respectively. For constant advection, N_c and N_c^f are taken to be the minimum number of quadrature points required to integrate the mass matrix exactly.¹ We adopt this minimal quadrature rule, which is defined on the bi-unit cube using a $(N+1)^2$ point tensor product Gauss-Legendre quadrature in the a, b coordinates and an $(N+1)$ point Gauss-Jacobi quadrature with weights $(2, 0)$ in the c direction. The resulting points are then mapped using the Duffy-type transform to the bi-unit pyramid. We note that the integrals of derivatives of rational basis functions on the pyramid may be computed exactly using the minimal quadrature rule due to cancellation of the rational Jacobian factors with change of variables factors for the derivative. For $\alpha \in [0, 1]$ and periodic boundary conditions, the DG formulation is energy stable [14].

The resulting system of ODEs may then be solved in time using a method of lines discretization, such as low-storage 4th order Runge-Kutta [6]. For DG on affine-mapped simplicial elements, each physical mass matrix is a constant scaling of the reference mass matrix, and M^{-1} may be precomputed on the reference element and premultiplied with the lift and weak derivative matrices. For DG on pyramids, the mass matrix differs on each element, but is diagonal under the semi-nodal pyramid basis. Thus, instead of precomputing individual operators for each element, we precompute the diagonal factors of M^{-1} and apply them at each timestep.

4.2. GPU acceleration. Typical GPU-accelerated implementations break up the solution of the system of ODEs resulting from the DG discretization into three steps: computation of volume integrals, surface integrals, and a Runge-Kutta update step, which are performed by `VolumeKernel`, `SurfaceKernel`, and `UpdateKernel`, respectively:

$$\underbrace{\frac{du}{dt} + M^{-1}}_{\text{UpdateKernel}} \left(\underbrace{\sum_{k=1}^3 S^k u}_{\text{VolumeKernel}} + \underbrace{L^f F}_{\text{SurfaceKernel}} \right) = 0.$$

¹Non-constant advection is treated identically, though it may be beneficial to increase the number of quadrature points in order to offset under-integration (aliasing) effects.

This implementation differs slightly from simpler GPU-accelerated implementations of DG methods, in that `UpdateKernel`, in addition to advancing forward in time, applies the inverse of the mass matrix and interpolates the solution to surface cubature points. Work is partitioned such that elements (or batches of elements) are assigned to independent work-groups, while each work-item/thread processes work for either a single basis function or cubature node.

We consider first, for simplicity of presentation, a purely modal DG method for the pure convection equation with $\beta = [1, 0, 0]^T$, and outline the approach used to implement a solver on the GPU. The resulting system of equations for this specific constant advection problem is then

$$\frac{du}{dt} + M^{-1} (S^x u + L^f F) = 0, \quad L_{ij}^f = \int_{\partial K} n_x \phi_i(x) \phi_j(x) dx, \quad S_{ij}^x = \int_K \phi_i(x) \frac{\partial \phi_j}{\partial x} dx.$$

Algorithm 1 Computation of volume integrals.

1: **procedure** VOLUME KERNEL

2: Compute derivatives at cubature points \mathbf{x}_i for $i = 1, \dots, N_c$.

$$\frac{\partial u(\mathbf{x}_i)}{\partial x} = \sum_{j=1}^{N_p} \left(D_{ij}^r u_j \frac{\partial r(\mathbf{x}_i)}{\partial x} + D_{ij}^s u_j \frac{\partial s(\mathbf{x}_i)}{\partial x} + D_{ij}^t u_j \frac{\partial t(\mathbf{x}_i)}{\partial x} \right).$$

3: Scale by premultiplied values of $w_i J_i$, compute integral by multiplying by V^T .

$$\int_K \phi_i \frac{\partial u}{\partial x} = \sum_{i=1}^{N_c} V_{ji}^T w_i J_i \frac{\partial u(\mathbf{x}_i)}{\partial x}$$

4.2.1. Volume kernel. The computation of volume integrals requires evaluation of solution values at cubature nodes and computation of quadrature sums. We assume, for the reference pyramid, N_c volume cubature points r_i, s_i, t_i and weights w_i . Let V represent the volume Vandermonde matrix, and let D^r, D^s, D^t represent the derivative matrices with respect to reference coordinates r, s, t :

$$V_{ij} = \phi_j(r_i, s_i, t_i), \quad D_{ij}^r = \frac{\partial \phi_j(r_i, s_i, t_i)}{\partial r}, \quad D_{ij}^s = \frac{\partial \phi_j(r_i, s_i, t_i)}{\partial s}, \quad D_{ij}^t = \frac{\partial \phi_j(r_i, s_i, t_i)}{\partial t}.$$

We store the above $N_c \times N_p$ matrices, as well as V^T , only for the reference element. By storing geometric change-of-variables factors $\frac{\partial r}{\partial x}, \frac{\partial r}{\partial y}, \frac{\partial r}{\partial z} \dots$ and determinants $|J_i|$ of Jacobian mappings at the N_c volume cubature points at each element, we may compute the integral

$$(S^x u)_i = \int_K \phi_i \frac{\partial u}{\partial x} dx dy dz = \int_{\hat{K}} \phi_i(r, s, t) \left(\frac{\partial u}{\partial r} \frac{\partial r}{\partial x} + \frac{\partial u}{\partial s} \frac{\partial s}{\partial x} + \frac{\partial u}{\partial t} \frac{\partial t}{\partial x} \right) J dr ds dt$$

using V, D^r, D^s, D^t and the Jacobian factors premultiplied by quadrature weights $w_i J_i$, as described in Algorithm 1.

4.2.2. Surface Kernel. We assume N_c^f total surface cubature points (over all the faces of the pyramid) r_i^f, s_i^f, t_i^f with surface cubature weights w_i^f , and we define V^f as the surface Vandermonde matrix $V_{ij}^f = \phi_j(r_i^f, s_i^f, t_i^f)$. Storing normals $n_{x,i}, n_{y,i}, n_{z,i}$ and determinants of Jacobian mappings J_i^f at surface cubature points $\hat{\mathbf{x}}_i^f$, we may compute surface integrals of the flux F

$$(L^f F)_i = \int_{\partial K} \phi_i F dx, \quad F = (n_x - \alpha |n_x|) \llbracket u \rrbracket,$$

as described in Algorithm 2. This approach differs slightly from that of standard nodal DG algorithms in that it does not loop over faces, but computes over all cubature points on the surface of a pyramid at

once. This is due to the inhomogeneous nature of the faces on a pyramid — while it is possible to use low-memory techniques (discussed in more detail in Section 4.4) to compute surface integrals on triangular and quadrilateral faces, they require differentiation between the types of faces within a kernel, or separate kernels for triangular and quadrilateral faces.

Algorithm 2 Computation of surface integrals.

- 1: **procedure** SURFACE KERNEL
- 2: Compute flux $F = (n_x - \alpha |n_x|) \llbracket u \rrbracket$ at face cubature points, scale by surface Jacobian factors and weights J^f, w^f .

$$w_i^f J_i^f F_i.$$

- 3: Compute integral by multiplying by $(V^f)^T$

$$(L^f F)_i = \int_{\partial K} \phi_i F(u_f) = \sum_{i=1}^{N_e} (V^f)_{ji}^T w_i^f J_i^f F_i.$$

4.2.3. Update Kernel. Given the diagonal entries of the mass matrix, the timestep dt , and the k th step RK coefficients r_a^k, r_b^k , the update kernel inverts the mass matrix, performs both a Runge-Kutta substep to march the solution to the next time, and interpolates the new solution to surface cubature nodes for use in the next surface kernel, as shown in Algorithm 3.

Algorithm 3 Runge-Kutta update step with added interpolation to face cubature points.

- 1: **procedure** RUNGE-KUTTA UPDATE STEP
- 2: Compute right-hand side

$$b_i^k = \frac{1}{M_{ii}} b_i,$$

where b_i is the sum of volume and surface integrals.

- 3: Update residual r and local solution at the k th RK step

$$r_i = r_a^k r_i + dt b_i^k, \quad u_i^k = u_i + r_b^k r_i.$$

- 4: Interpolate local solution to face cubature points using the face Vandermonde matrix V^f .

$$u^{f,k} = V^f u^k.$$

4.2.4. Kernel optimization. We attempted to optimize the above kernels by minimizing the number of memory accesses, minimizing non-unit strided memory accesses, maximizing the speed at which data is accessed, or hiding the effect of latency in accessing data.

When data must be accessed repeatedly, we take advantage of the GPU memory hierarchy. Data that is used repeatedly within a workgroup is loaded to shared memory, and data used repeatedly in threads is loaded to register memory, both of which allow for fast data retrieval.² Likewise, since register memory is limited, multiple inputs are concatenated into strided arrays in order to decrease register pressure.

Finally, we may hide the latency present in memory accesses by exploiting work which may be done concurrently. For example, we may prefetch values (such as geometric factors in the computation of volume

²Since the shared memory available on GPUs is limited, using a large amount shared memory in a kernel will reduce the number of concurrent active work groups, so we do not load derivative matrices and interpolation operators to shared memory due to their large number of entries in 3D. These matrix reads are still relatively efficient due to coalescing and caching effects.

AMD	AMD Tahiti + OpenCL
Nvidia	Nvidia GeForce GTX 980 + CUDA
CPU	Intel Core i7-5960X + OpenMP

TABLE 4.1

Legend of abbreviations for different computational architectures.

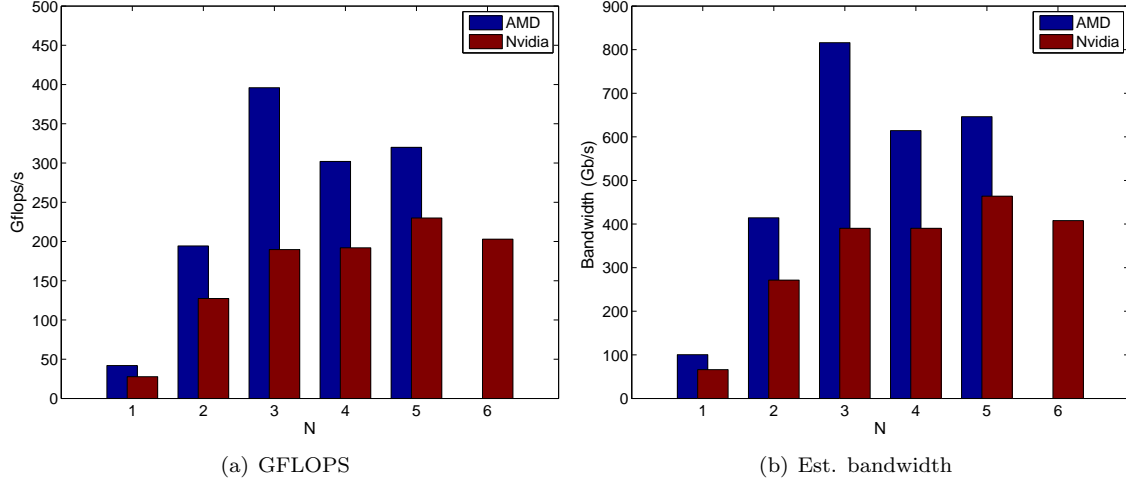


FIG. 4.1. *GFLOPS and estimated effective bandwidth for the advection volume kernel under both the AMD and Nvidia setup.*

integrals) before executing other independent commands. Additionally, prefetching may facilitate additional compiler optimizations; though the volume kernel achieves roughly the same performance with and without prefetching under CUDA, the volume kernel with prefetching achieves an extra 10-25 GFLOPS when running under OpenCL.

To assess the computational performance of the semi-nodal pyramid basis, we implemented a GPU-accelerated DG solver using the OCCA scripting language [19]. The solver is written using OCCA kernels, which may then be expanded to various threading languages for portability across differing architectures. Numerical experiments suggest that OCCA kernels, translated into CUDA, OpenCL, or OpenMP, perform nearly as well as hand-tuned kernels written directly in the native language [10]. The DG solver is run for a fixed number of timesteps on an Nvidia GeForce GTX 980 using CUDA (which we abbreviate as “Nvidia”) and an AMD Tahiti GPU using OpenCL (which we abbreviate as “AMD”). Additionally, we ran the same kernels up to $N = 4$ on an Intel Core i7-5960X CPU using OpenMP (which we abbreviate as “CPU”). The GFLOPS and estimated effective bandwidth of each kernel are reported in Figure 4.4. We note that the effective bandwidth estimates do not consider caching effects; as a result, the reported numbers may exceed the maximum available device bandwidth. Table 4.1 gives a legend of abbreviations and their respective computational platforms.

The mesh is taken to be a $16 \times 16 \times 16$ mesh of hexahedral elements, each of which is then subdivided into 6 pyramids to produce 24576 elements. The order is varied from $N = 1$ to $N = 6$ (order is limited to $N = 5$ when using OpenCL, due to the memory limitations on workgroup size), and both GFLOPS and estimated effective bandwidth (averaged over three runs) are reported for the volume and surface kernels in Figures 4.1, 4.2, and 4.3.

We note that the effect of caching is relatively significant in computing estimated bandwidth. If the bandwidth is estimated without counting operator loads, we get

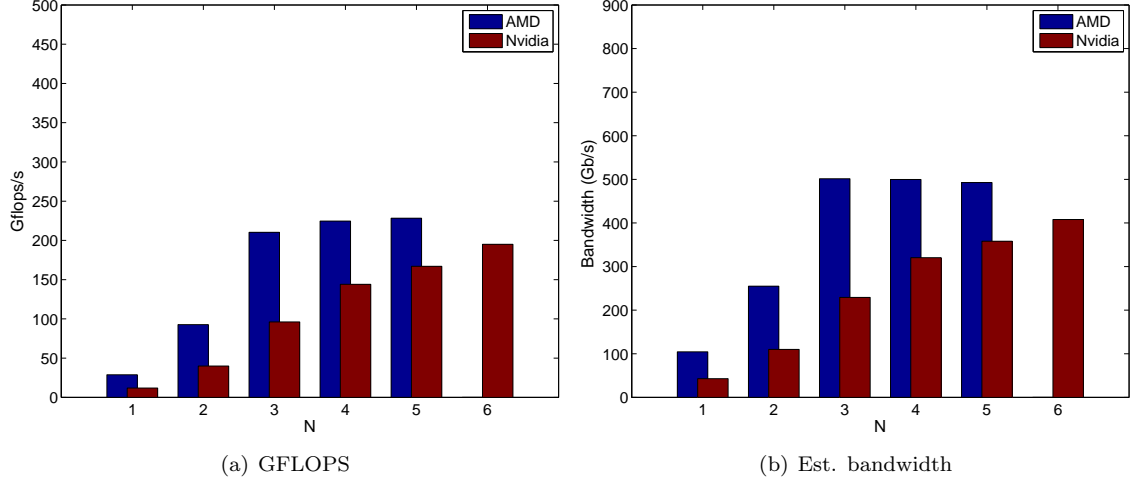


FIG. 4.2. *GFLOPS and estimated effective bandwidth for the advection surface kernel under both the AMD and Nvidia setup.*

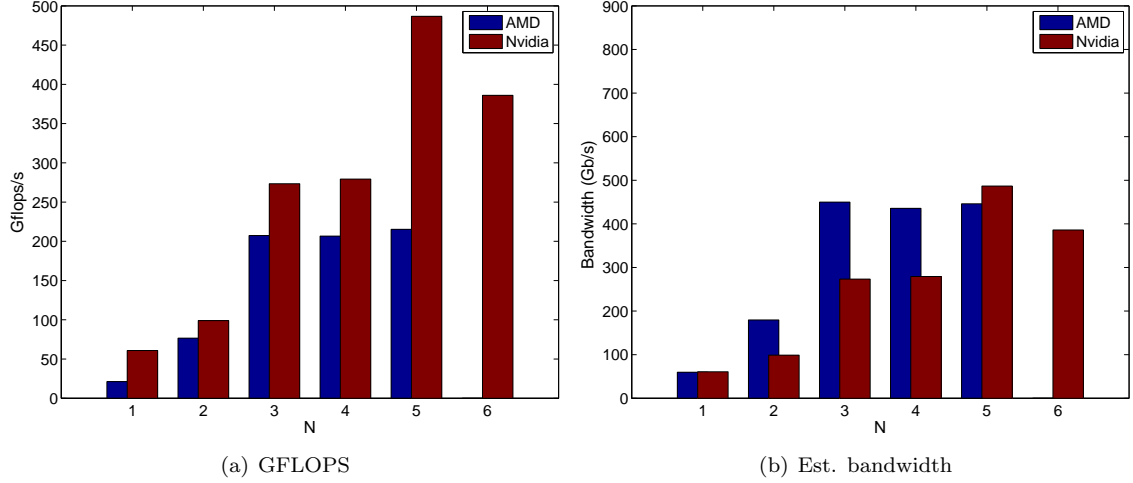


FIG. 4.3. *GFLOPS and estimated effective bandwidth for the advection RK update kernel under both the AMD and Nvidia setup.*

4.3. Acoustic wave equation. We consider also the acoustic wave equation on domain Ω with free surface boundary conditions $p = 0$ on $\partial\Omega$. This may be written in first order form

$$\begin{aligned} \frac{1}{\kappa} \frac{\partial p}{\partial t} + \nabla \cdot \mathbf{u} &= f \\ \rho \frac{\partial \mathbf{u}}{\partial t} + \nabla p &= 0, \end{aligned}$$

where p is acoustic pressure, \mathbf{u} is velocity, and ρ and κ are density and bulk modulus, respectively, and are assumed to be piecewise constant.

Let (p^-, \mathbf{u}^-) denote the solution fields on the face of an element K , and let (p^+, \mathbf{u}^+) denote the solution on the neighboring element adjacent to that face. Defining the jump of p and the vector velocity \mathbf{u} componentwise

$$[\![\mathbf{u}]\!] = \mathbf{u}^+ - \mathbf{u}^-, \quad [\![p]\!] = p^+ - p^-,$$

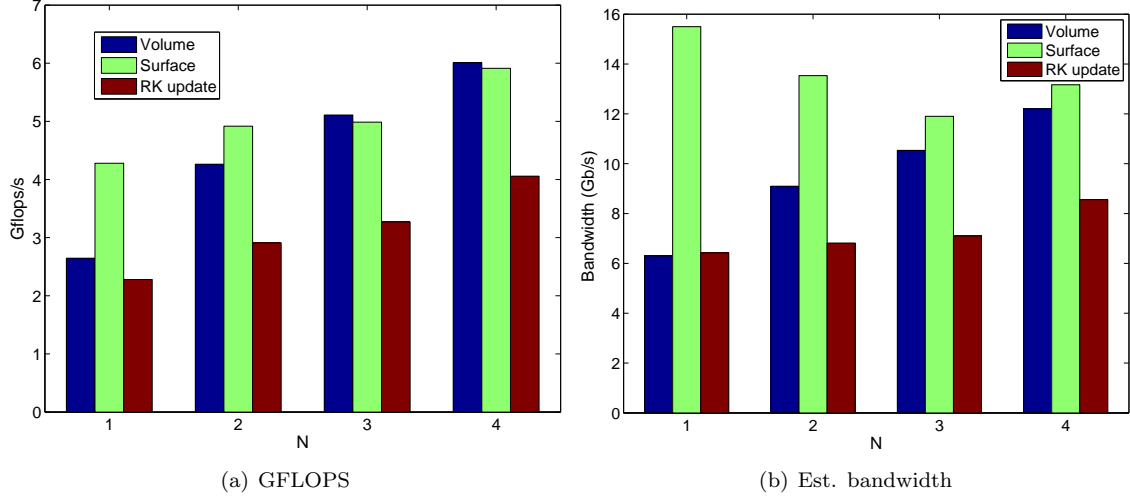


FIG. 4.4. *Gflops and estimated effective bandwidth for advection volume, surface, and update kernels under the CPU setup.*

the semi-discrete variational formulation for the discontinuous Galerkin method may then be given over an element as

$$\begin{aligned} \int_K \left(\frac{1}{\kappa} \frac{\partial p}{\partial t} + \nabla \cdot \mathbf{u} \right) v^- \, dx + \int_{\partial K} \frac{1}{2} (\mathbf{n} \cdot [\mathbf{u}] - \tau_p \llbracket p \rrbracket) v^- \, dx &= \int_K f v^- \, dx \\ \int_K \left(\rho \frac{\partial \mathbf{u}}{\partial t} + \nabla p \right) v^- + \int_{\partial K} \mathbf{n} \frac{1}{2} (\llbracket p \rrbracket - \tau_u \mathbf{n} \cdot [\mathbf{u}]) v^- \, dx &= 0, \end{aligned}$$

where $\tau_p = 1/\{\llbracket \rho c \rrbracket\}$, $\tau_u = \{\llbracket \rho c \rrbracket\}$, and $c^2 = \kappa/\rho$ is the speed of sound.

We discretize by again representing \mathbf{u}, v using the semi-nodal basis ϕ_{ijk} . This converts the variational problem into a system of ODEs

$$\begin{aligned} \frac{dp}{dt} + \kappa M^{-1} \left(\sum_{k=1}^3 S^k u_k + L^f P_p \right) &= b, \\ \frac{du_k}{dt} + \rho M^{-1} (S^k u_k + L^{f,k} P_{u_k}) &= 0, \quad k = 1, \dots, 3, \end{aligned}$$

where L^f is the scalar lift operator, and $L^{f,k}$ is the vector lift operator defined by

$$L_{ij}^{f,k} = \int_{\partial K} \mathbf{n}_k \phi_i(x) \phi_j(x) \, dx \approx \sum_{l=1}^{N_c^f} w_l \phi_i(x_l) \phi_j(x_l)$$

applied to the penalty terms P_p, P_{u_i} , and S^k is the weak derivative matrix defined by

$$S_{ij}^k = \int_K \frac{\partial \phi_j}{\partial x_k} \phi_i(x) \, dx \approx \sum_{l=0}^{N_c} w_l \frac{\partial \phi_j(x_l)}{\partial x_k} \phi_i(x_l)$$

for an appropriate N_c point quadrature rule with points x_l and weights w_l .

Defining a vector variable $\mathbf{U} = (p, \mathbf{u})$, we may write our system of ODEs for the wave equation as

$$\frac{d\mathbf{U}}{dt} = \mathbf{A}\mathbf{U}.$$

The computed spectral radii of the RHS matrix $\rho(\mathbf{A})$ are given in Figure 4.5 for various mesh sizes h (computed as the ratio of surface area to volume of an element) and a function of the order of approximation

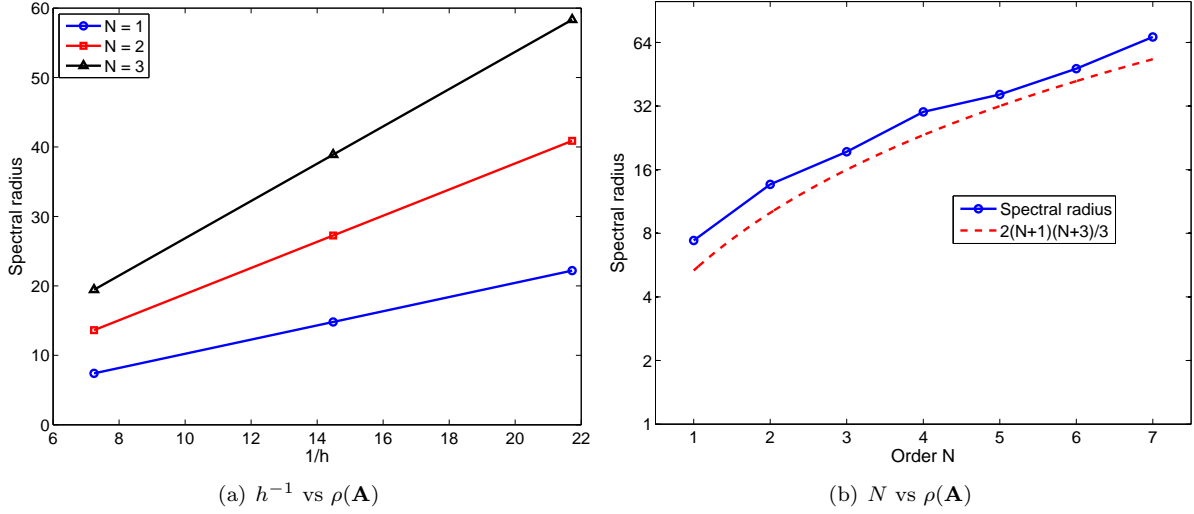


FIG. 4.5. Ratio of numerically computed spectral radii $\rho(\mathbf{A})$, plotted against both mesh size h and $2(N+1)(N+3)/3$.

N . The spectral radius $\rho(\mathbf{A})$ gives an estimate of the maximum timestep under which an explicit scheme remains stable, and for standard polynomial finite element spaces is proportional to N^2/h . We observe the same behavior numerically for pyramids, and note that the spectral radius shows very good agreement with $2(N+1)(N+3)/3$, which is the N -dependent constant in the discrete trace inequality for the pyramid [8].³

We also report numerical convergence rates in Figure 4.6 for the resonant cavity solution

$$p(x, y, z, t) = \cos(\pi x/2) \cos(\pi y/2) \cos(\pi z/2) \cos(\sqrt{3}\pi t/2).$$

over the bi-unit cube $[-1, 1]^3$. Meshes are again constructed by subdividing the cube into $K_{1D} \times K_{1D} \times K_{1D}$ hexahedra, which are then each subdivided into 6 pyramids. Pyramid vertex positions are perturbed to ensure J is non-constant in each element.

It was confirmed in [3] that the rational basis (2.1) achieves optimal $O(N+1)$ rates of convergence for both the L^2 and dispersion error. Since the basis defined by ϕ_{ijk} spans the same approximation space as that of (2.1), the numerical errors and convergence rates are also of optimal order, and we observe both optimal rates of convergence in h and exponential convergence in N . The errors are computed in double precision on the GPU; when using single precision, the convergence rates behave similarly, but L^2 errors stall at around 10^{-6} due to finite precision effects.

We present GFLOPS and estimated effective bandwidth for the volume, surface, and RK update kernel in Figures 4.7, 4.8, and 4.9. While the estimated effective bandwidth for acoustic wave kernels is similar to that of the advection kernels, the GFLOPS have increased by a factor of 2-4, due to the reuse of derivative and interpolation operators over multiple field variables. This may be further confirmed by examining the estimated effective bandwidth without counting operator loads, in which case the reported bandwidth decreases by roughly an order of magnitude.

Figure 4.10 shows GFLOPS and estimated effective bandwidth on an Intel Core i7-5960X CPU using OpenMP. Again, the GFLOPS of acoustic wave kernels increase while the estimated effective bandwidth remains roughly the same as that of the advection kernels, though the increase is not as pronounced as the increase in GFLOPS from advection to the acoustic wave equation on the GPU.

4.4. Computational improvements. Despite the reported GFLOPS and estimated effective bandwidth reported for pyramids above, it is possible to improve the efficiency of DG on pyramids further.

³Though the meshes used to compute the spectral radii are uniform, randomly perturbing the vertex positions does not change the value of $\rho(\mathbf{A})$ significantly, which was also observed in [3].

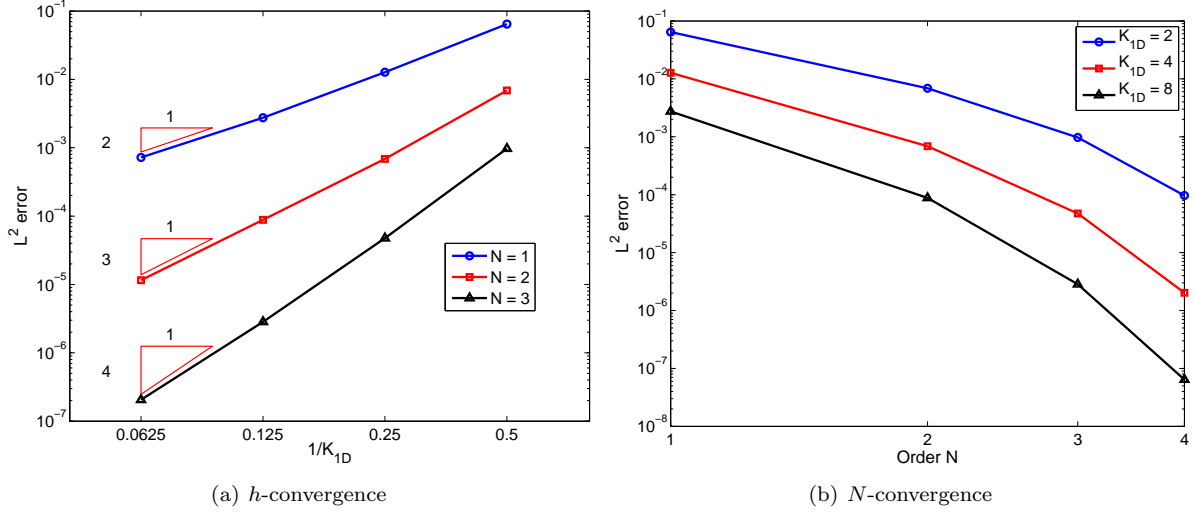


FIG. 4.6. Computed L^2 errors for various orders N and mesh sizes, with optimal rates of h -convergence for reference.

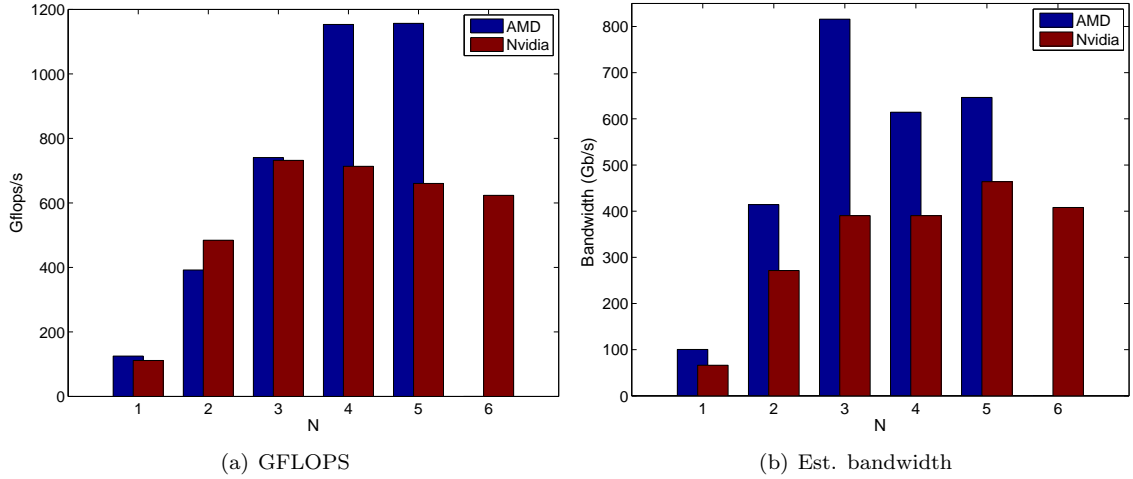


FIG. 4.7. GFLOPS and estimated effective bandwidth for the wave volume kernel under both the AMD and Nvidia setup.

4.4.1. Nodal basis functions. In the above discussions, we discretize by taking the orthogonal (modal) basis ϕ_{ijk} defined in Lemma 2.3). However, switching to a nodal discretization using Lagrange basis functions at N_p distinct points on the pyramid requires only a small modification in the application of the mass matrix inverse. Instead of inverting a diagonal matrix, may be inverted by a change of basis from a nodal to the orthogonal semi-nodal basis. It is often desirable to define nodal basis functions at strong interpolation points with respect to the Lebesgue constant, which is present in upper bounds on the interpolation error in the maximum norm. Additionally, for meshes containing multiple element types, it is convenient to choose nodal points on the triangular faces with $(N+1)(N+2)/2$ points on the triangular faces and $(N+1)^2$ points on the quadrilateral face such that the distribution on those faces matches the distribution on the faces of either hexahedra or tetrahedra. A survey of various nodal points for the pyramid with both low Lebesgue constant and appropriate nodal distributions on faces is given in [7].

If the triangular and quadrilateral faces of all elements in a mesh share the same symmetric nodal distribution, conformity under continuous Galerkin methods may be enforced simply by matching the nodal degrees of freedom on the faces of adjacent elements, and the computation of surface integrals may be

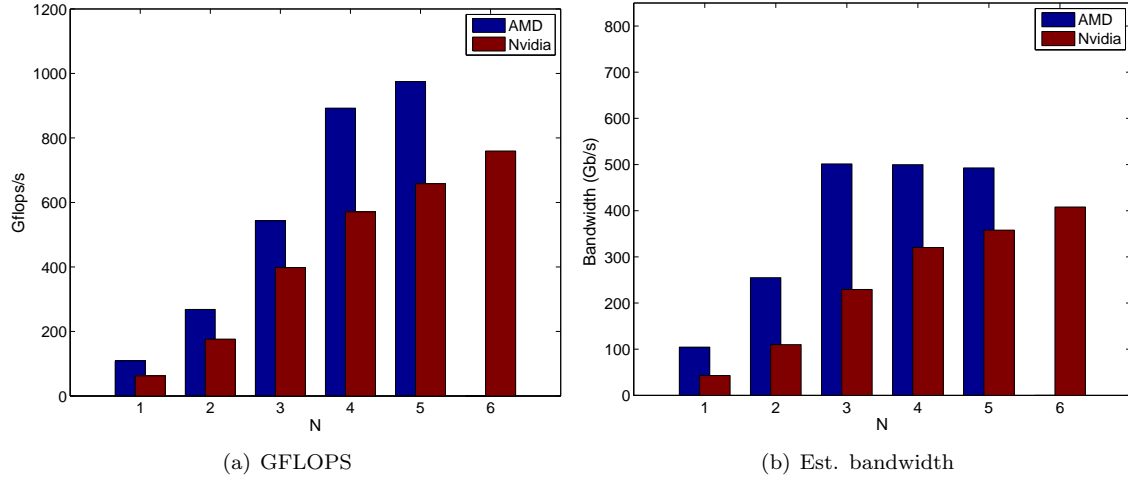


FIG. 4.8. *GFLOPS and estimated effective bandwidth for the wave surface kernel under both the AMD and Nvidia setup.*

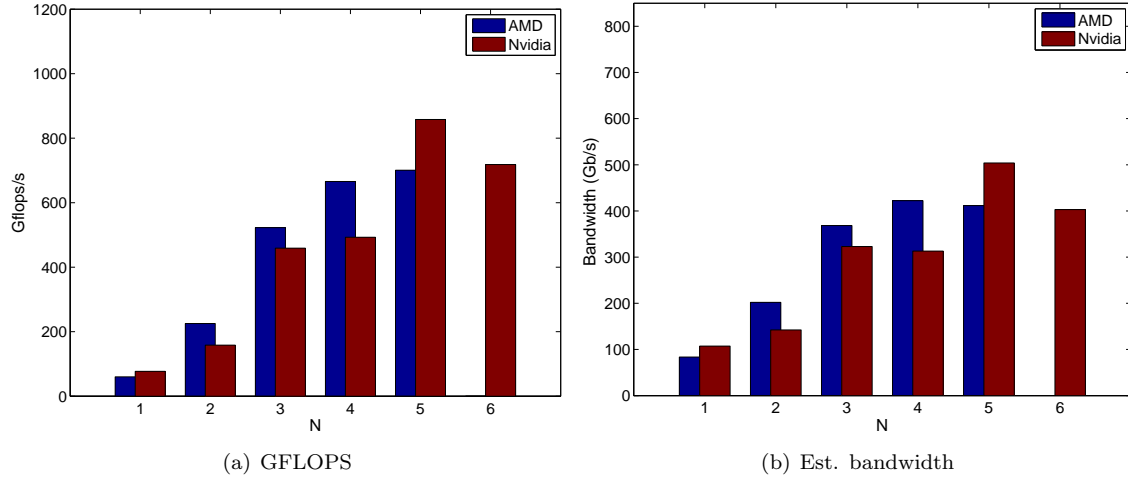


FIG. 4.9. *GFLOPS and estimated effective bandwidth for the wave RK update kernel under both the AMD and Nvidia setup.*

simplified. In particular, for discontinuous Galerkin methods on vertex-mapped pyramids, surface integrals may be computed using only nodal degrees of freedom on a face and face mass matrices. For triangular faces, the face mass matrices are scalings of the reference nodal face mass matrix, and the quadrilateral face mass matrix may be expressed as the Kronecker product of separable scalings of 1D nodal mass matrices. As a result, the use of nodal mass matrices is more efficient and requires less memory than the use of quadrature for the computation of surface integrals. Since the computation of surface integrals is the dominant cost for low order discontinuous Galerkin methods, nodal methods are often observed to be more efficient for moderate values of N [4, 14]. For larger values of N , the ratio of interior degrees of freedom to surface degrees of freedom increases, and the cost of computing volume integrals becomes dominant.

4.4.2. Volume kernel evaluation. While the computation of surface integrals may also be performed using mass matrices under a nodal basis, volume integrals must still be computed using quadrature due to the the rational nature of the mapping. Despite the reported GFLOPS and estimated effective bandwidth, the cost of the volume kernel becomes a limiting factor at high orders. Figure 4.11 shows reported runtimes

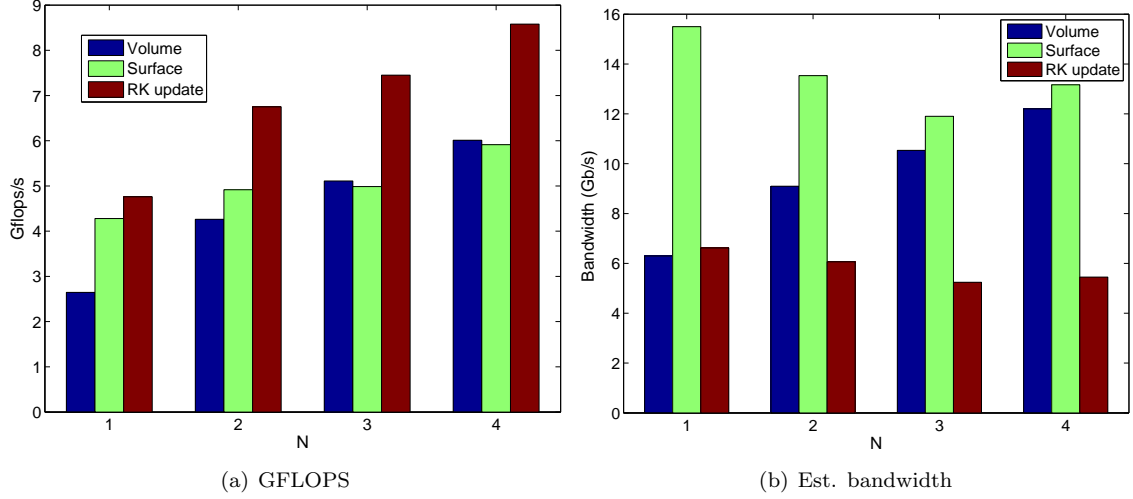


FIG. 4.10. *Gflops and estimated effective bandwidth for wave volume, surface, and update kernels under the CPU setup.*

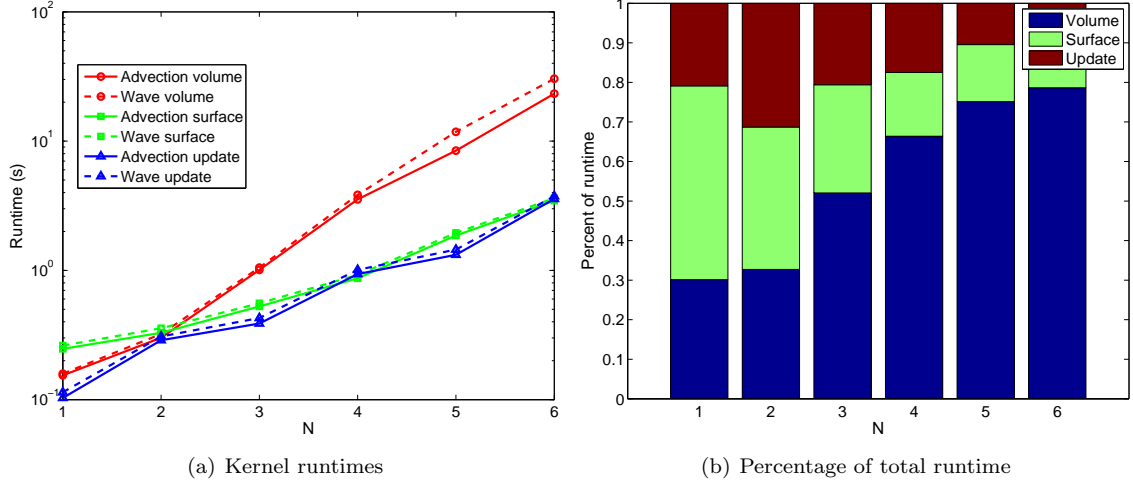


FIG. 4.11. *Runtimes and average percentage of total runtime for each individual kernel.*

and percentage of total runtimes⁴ for volume, surface, and update kernels on an Nvidia GeForce GTX 980 over 100 timesteps; at $N > 2$, the volume kernel becomes the dominating bottleneck due to use of tensor product cubature rules for the pyramid, which results in an $O(N^6)$ cost in applying derivative operators, in contrast to $O(N^4)$ cost of surface cubature and applying interpolation operators in the surface and update kernels, respectively.

This cost may be alleviated by exploiting the tensor-product nature of the orthogonal pyramid basis and quadrature rule. This was done by Bergot, Cohen, and Durufle in [4] to yield lower-cost evaluations of volume integrals for the non-orthogonal pyramid basis. It may also be possible to decrease memory costs and improve efficiency by adopting quadrature rules constructed directly on the pyramid instead of mapping quadrature rules from the bi-unit cube to the pyramid, which typically involve a fewer number of points than the $(N + 1)^3$ -point rules currently used [18, 27]. We hope to explore these options in future work.

⁴The percentage of total runtimes are averages of the percentage of total runtime for advection kernels and percentage of total runtime for wave kernels.

5. Conclusions and acknowledgements. We have presented a new higher order basis which is orthogonal on vertex-mapped transformations of the reference pyramid, despite the fact that the transformation is non-affine. This allows for low-storage implementations of discontinuous Galerkin methods on pyramids, which we hope will aid efficient GPU implementations on hex-dominant meshes.

The work of the first author (JC) was supported partially by the Rice University CAAM Department Pfeffer Postdoctoral Fellowship. The second author (TW) was supported partially by ANL (award number 1F-32301, subcontract on DOE DE-AC02-06CH11357). Both authors would like to acknowledge the support of NSF (award number DMS-1216674) in this research. The authors would additionally like to thank David Medina and Rajesh Gandham for helpful discussions during the writing of this manuscript.

REFERENCES

- [1] Tristan Carrier Baudouin, Jean-François Remacle, Emilie Marchandise, François Henrotte, and Christophe Geuzaine. A frontal approach to hex-dominant mesh generation. *Advanced Modeling and Simulation in Engineering Sciences*, 1(1):1–30, 2014.
- [2] G Bedrosian. Shape functions and integration formulas for three-dimensional finite element analysis. *International journal for numerical methods in engineering*, 35(1):95–108, 1992.
- [3] Morgane Bergot, Gary Cohen, and Marc Duruflé. Higher-order finite elements for hybrid meshes using new nodal pyramidal elements. *Journal of Scientific Computing*, 42(3):345–381, 2010.
- [4] Morgane Bergot and Marc Duruflé. Higher-order discontinuous galerkin method for pyramidal elements using orthogonal bases. *Numerical Methods for Partial Differential Equations*, 29(1):144–169, 2013.
- [5] Sven Beuchler and Joachim Schoeberl. New shape functions for triangular p-FEM using integrated Jacobi polynomials. *Numerische Mathematik*, 103(3):339–366, 2006.
- [6] Mark H Carpenter and Christopher A Kennedy. Fourth-order $2n$ -storage Runge-Kutta schemes. Technical Report NASA-TM-109112, NAS 1.15:109112, NASA Langley Research Center, 1994.
- [7] Jesse Chan and T Warburton. A comparison of high order interpolation nodes for the pyramid. *arXiv preprint arXiv:1412.4138*, 2014.
- [8] Jesse Chan and T Warburton. hp-finite element trace inequalities for the pyramid. *Computers & Mathematics with Applications*, 2015.
- [9] Leszek Demkowicz, Jason Kurtz, David Pardo, Maciej Paszynski, Waldemar Rachowicz, and Adam Zdunek. *Computing with Hp-Adaptive Finite Elements, Vol. 2: Frontiers Three Dimensional Elliptic and Maxwell Problems with Applications*. Chapman & Hall/CRC, 1st edition, 2007.
- [10] Rajesh Gandham, DS Medina, and Timothy Warburton. GPU accelerated discontinuous Galerkin methods for shallow water equations. *arXiv preprint arXiv:1403.1661*, 2014.
- [11] Gregor J Gassner, Frieder Lörcher, Claus-Dieter Munz, and Jan S Hesthaven. Polymorphic nodal elements and their application in discontinuous Galerkin methods. *Journal of Computational Physics*, 228(5):1573–1590, 2009.
- [12] Gene H Golub and Richard S Varga. Chebyshev semi-iterative methods, successive overrelaxation iterative methods, and second order Richardson iterative methods. *Numerische Mathematik*, 3(1):157–168, 1961.
- [13] Brian T Helenbrook. On the existence of explicit hp-finite element methods using Gauss-Lobatto integration on the triangle. *SIAM Journal on Numerical Analysis*, 47(2):1304–1318, 2009.
- [14] Jan S Hesthaven and Tim Warburton. *Nodal discontinuous Galerkin methods: algorithms, analysis, and applications*, volume 54. Springer, 2007.
- [15] George Karniadakis and Spencer J Sherwin. *Spectral/hp Element Methods for CFD*. Oxford University Press, 1999.
- [16] Andreas Klöckner, Tim Warburton, Jeff Bridge, and Jan S Hesthaven. Nodal discontinuous galerkin methods on graphics processors. *Journal of Computational Physics*, 228(21):7863–7882, 2009.
- [17] Lilia Krivodonova and Marsha Berger. High-order accurate implementation of solid wall boundary conditions in curved geometries. *Journal of computational physics*, 211(2):492–512, 2006.
- [18] Ethan J Kubatko, Benjamin A Yeager, and Ashley L Maggi. New computationally efficient quadrature formulas for triangular prism elements. *Computers & Fluids*, 73:187–201, 2013.
- [19] David S Medina, Amik St-Cyr, and T Warburton. OCCA: A unified approach to multi-threading languages. *arXiv preprint arXiv:1403.0968*, 2014.
- [20] William A Mulder. New triangular mass-lumped finite elements of degree six for wave propagation. *Progress in Electromagnetics Research PIER*, (141) 2013, 2013.
- [21] Nilima Nigam and Joel Phillips. High-order conforming finite elements on pyramids. *IMA Journal of Numerical Analysis*, 32(2):448–483, 2012.
- [22] Nilima Nigam and Joel Phillips. Numerical integration for high order pyramidal finite elements. *ESAIM: Mathematical Modelling and Numerical Analysis*, 46(02):239–263, 2012.
- [23] Joachim Schöberl, H Gerstmayr, and R Gaisbauer. Netgen-automatic mesh generator, 2012.
- [24] T Warburton. A low storage curvilinear discontinuous Galerkin time-domain method for electromagnetics. In *Electromagnetic Theory (EMTS), 2010 URSI International Symposium on*, pages 996–999. IEEE, 2010.
- [25] Timothy Warburton. A low-storage curvilinear discontinuous Galerkin method for wave problems. *SIAM Journal on Scientific Computing*, 35(4):A1987–A2012, 2013.
- [26] Andrew J Wathen and Tyrone Rees. Chebyshev semi-iteration in preconditioning for problems including the mass matrix.

- Electronic Transactions on Numerical Analysis*, 34:125–135, 2009.
- [27] FD Witherden and PE Vincent. On the identification of symmetric quadrature rules for finite element methods. *arXiv preprint arXiv:1409.1865*, 2014.
- [28] S. Zaglmayr. *High Order Finite Element Methods for Electromagnetic Field Computation*. PhD thesis, Johannes Kepler University, 2006.